Solar Physics
DOI: 10.1007/•••••-•••-•••-••••-•

# Analysis and Characterization of SPT-3G Multiplexing Readout Electronics

**Taryn Imamura[1,2,3] · Supervisor:**
**Bradford Benson[1,3,4] · Supervisor:**
**Sasha Rahlin[3,4] · Supervisor:**
**Adam Anderson[3,4]**



**Abstract** The South Pole Telescope (SPT) is a cosmological collaboration located at the NSF Amundsen-Scott South Pole Station aimed towards measuring temperature anisotropies in the Cosmic Microwave Background (CMB). SPT's third generation camera (SPT-3G) increases the number of focal plane detectors and utilizes an fMux readout to achieve a faster mapping speed and higher resolution imaging of the millimeter wavelength sky. Before these detectors can be installed at the South Pole, they are tested at Fermi National Accelerator Laboratory (FNAL) to ensure they behave as specified and to identify the ideal parameters at which the detectors operate. Superconducting Quantum Interference Device (SQUID) and Inductance-Capacitance filter networks (LC) were tested using a cryostat, network analyses, and python algorithms. Their data was then recorded and compared to expected values. Ultimately, five SQUIDs were flagged as defective and removed from use on SPT-3G. Additionally, the ideal operating currents and signal frequencies for each SQUID and LC were identified and recorded for use at the South Pole.

**Keywords:** SPT-3G, CMB, FNAL, SQUIDs, fMux

✉ T.R.I. Imamura
taryni@stanford.edu

✉ B.B. Benson
http://kicp.uchicago.edu/ bbenson/

[1] Stanford University

[2] Summer Internships in Science and Technology (SIST) Intern

[3] Fermi National Accelerator Laboratory

[??] The South Pole Telescope

# 1. Background

## 1.1. The Cosmic Microwave Background

The information for this introduction was taken from Carlstrom, Crawford, and Knox 2018, which can be referenced for more in-depth background information.

The Cosmic Microwave Background (CMB) is electromagnetic radiation left over from the earliest event in our universe's history: the Big Bang (Carlstrom, Crawford, and Knox, 2018). The CMB was first discovered in 1964 when American radio astronomers Robert Wilson and Arno Penzias detected a mysterious excess noise emanating from all parts of the sky. After painstakingly eliminating all possible sources of instrumental noise, they concluded that they had accidentally made a scientific breakthrough. Penzias and Wilson won the 1978 Nobel Prize for their discovery, which forever intertwined cosmology and particle physics.

The CMB is the oldest visible light in the universe and dates back to 380,000 years after the Big Bang. Before this time, the universe was an extremely hot, opaque plasma of photons, electrons, and protons. This plasma was strongly coupled through photon-electron scattering and Coulomb interactions that impeded the movement of photons. After the Big Bang, the universe began cooling continuously as it expanded, and after 380,000 years, it cooled enough to allow the formation of electrically neutral particles such as Hydrogen. This event, known as "recombination," marked the first time CMB photons could travel through the universe. The CMB we observe today depicts the last scattering surface of the universe at the time of recombination and provides us with a visual snapshot of the earliest stages of our universe.

The CMB is extremely bright and uniform, with a temperature uniformity of about 1 part in 100,000 in every direction. The CMB temperature has been mapped by both satellite experiments and by ground-based telescopes such as the South Pole Telescope and the Atacama Cosmology Telescope. This uniformity supports the theory of cosmic inflation and suggests that the universe expanded much faster than the speed of light after the Big Bang (Benson *et al.*, 2014).

The study of the CMB by collaborations such as the South Pole Telescope (SPT) has lead to new discoveries in three main areas: measuring fine-scale CMB temperature anisotropy, detecting the first "B modes" in the polarization of the CMB, and using the SZ effect to discover new galaxy clusters (particularly at high redshift) (Benson *et al.*, 2014). I will further discuss B modes in Section 1.2.

## 1.2. CMB Polarization and Primordial Gravitational Waves

The information from this introduction came from (Krauss, Dodelson, and Meyer, 2010) which can be referenced for more in depth information.

As predicted by Einstein's theory of General Relativity, gravitational waves interact weakly with matter. As a result, they have traveled uninterrupted through the universe since the time of the Big Bang and can provide valuable insight into the early universe if we can detect them. Conveniently, gravitational waves can

be detected via measurement of polarization in the CMB. Gravitational waves, such as those observed by the Laser Interferometer Gravitational-Wave Observatory (LIGO) detector, originated from local space-time distortion caused by gravitational waves from astrophysical objects such as colliding neutron stars or black holes. However, another source of gravitational waves is the early expansion of the universe.

These primordial gravitational waves leave indirect traces in CMB anisotropy maps. Fluctuations in primordial mass and energy create observable CMB temperature anisotropies; however, primordial gravitational waves produce both temperature anisotropies and a distinct signal that can be detected in the CMB polarization. Although the CMB temperature anisotropies have been well mapped, experiments such as SPT-3G have been motivated in order to take sensitive measurements of the CMB polarization.

The CMB has a 10 percent polarization due to Thompson scattering of an anisotropic radiation background off of free electrons before the time of electron-proton recombination. This percentage means that observed photons have a larger intensity in a particular direction. Polarization can be represented using a vector field in which the polarization at every position is described by an amplitude and an angle of orientation. We can then decompose this vector field into two modes: curl-free E modes and divergence-free B modes. A diagram of these E and B modes is depicted in Figure 1. B modes cannot be produced by scalar perturbations and instead result from and are a signature of primordial gravitational waves. These gravitational waves are linked to inflation in the early universe. As a result, observing the B mode polarizations of the CMB would allow us to analyze the nature of the early universe prior to the epoch of recombination.

### 1.3. The South Pole Telescope

The South Pole Telescope (SPT) millimeter wavelength telescope designed to take higher resolution measurements of the CMB anisotropy (Bender *et al.*, 2016; Benson *et al.*, 2014). The SPT's classical Gregorian, off-axis design provide low scattering, high efficiency, and wide diffraction without blocking the main aperture (Benson *et al.*, 2014). The SPT takes measurements by rotating the entire telescope up to 4 deg/sec and operates remotely with high observing efficiency. The SPT is located at at the NSF Amundsen-Scott South Pole Station which is one of the best developed sites for mm-wave observation on Earth due to its low levels of atmospheric fluctuation power (Benson *et al.*, 2014).

The third-generation CMB receiver, SPT-3G, was recently installed on the SPT. TES detectors have reached the photon noise limit (shot noise), meaning that their noise performance results from fluctuations in the arrival rate of photons at the detectors as opposed to intrinsic noise in the detectors themselves (Dobbs *et al.*, 2012). As a result, higher mapping speed must be achieved by increasing the number of detectors instead of improving the detectors themselves. SPT-3G, the most recent SPT update, increases the telescope's focal plane size to approximately 16,000 bolometers, 10x the number of detectors as the CMB receiver that it replaced (SPTpol) (Bender *et al.*, 2016; Benson *et al.*, 2014). SPT-3G achieves a factor-of-10 increase in mapping speed through two primary

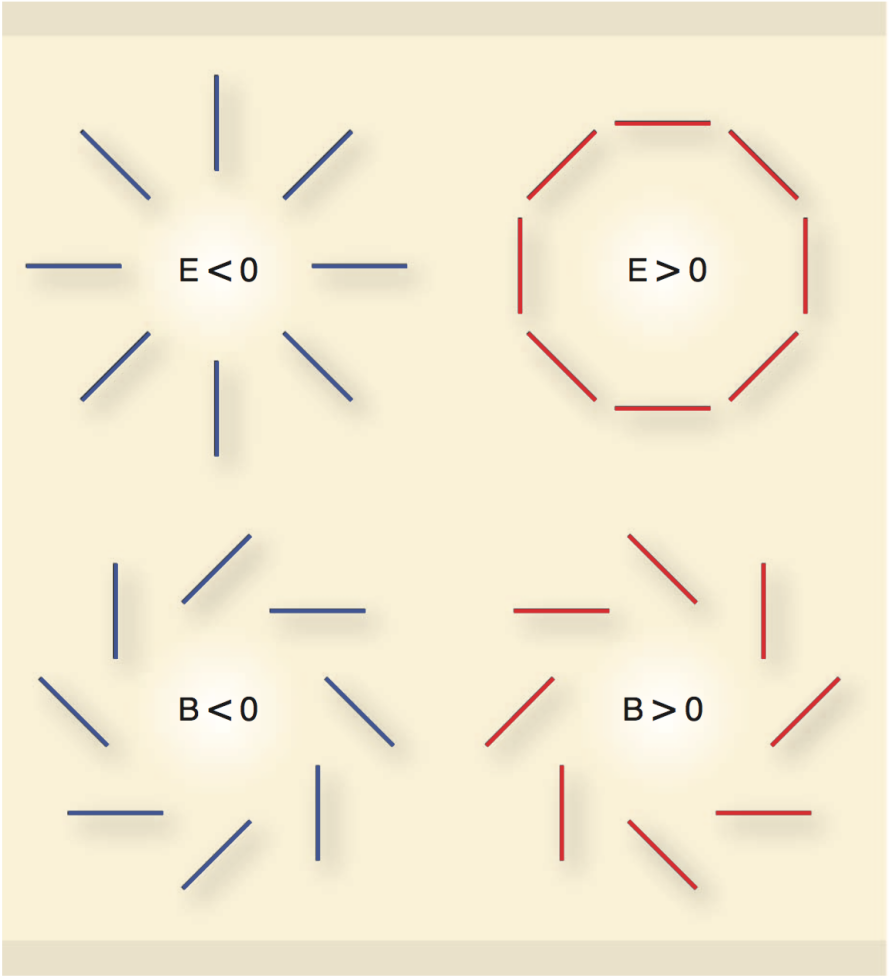


**Figure 1.** This figure shows the E and B modes of the CMB polarization that are used to measure gravitational waves.

technological advances: a wide-field optical design that increases the focal plane by more than twice as many diffraction-limited optical elements and the use of multi-chroic pixels that are sensitive to multiple observing bands for each single detector element (Benson *et al.*, 2014). In this paper, I will describe the testing and characterization of components of the multiplexing readout electronics.

### 1.4. Purpose and Motivation

The purpose of this project was to test and characterize multiplexing readout components for use on the South Pole Telescope. SPT detector components are heavily inter-reliant, meaning that one malfunctioning element early in the

circuit could result in poor data for all following channels. I will provide a more detailed introduction to the detector and its circuit in 2.

To test the system, we systematically isolated and analyzed the individual components of the circuit beginning with the SQUIDs followed by the LC boards and detector wafers. As we progressed, we connected each new component onto the preexisting circuit to observe their behavior as a unit. For the sake of readability, the data and discussion of this testing is segmented by component.

This project was motivated by the upcoming Austral summer and the maintenance opportunity it affords. During this time, researchers at the South Pole will have the opportunity to repair or replace worn-out components from the SPT-3G detector. As a part of the yearly replacement and upgrade, this project was meant to test these detectors and ensure that their operation was satisfactory before their transportation to the NSF Amundsen-Scott South Pole station. Additionally, we identified the operational parameters at which the performance of the readout electronics were optimized.

## 2. Introduction

### 2.1. SPT Detector

A detailed, 3D rendering of the SPT-3G detector wafer is shown in Figure 4. The SPT-3G detector consist of a focal plane with 271 multi-chroic pixels per wafer and 10 wafers in total. Each pixel contains 6 bolometers and a broadband sinuous antenna that is polarization-sensitive to the CMBs millimeter wavelength power (Bender *et al.*, 2016). This leads to a total of 16,000 bolometers. This pixel is shown in Figure 2. This power is distributed to the 6 bolometers, each of which consists of a suspended island with a resistor that absorbs power and a voltage biased TES to measure the island's temperature. Fluctuating levels of millimeter wavelength power from the sky heat the TES which changes its resistance. As the TES resistance changes, the amount of electrical power applied to the circuit changes through a negative feedback loop. This negative feedback loop is driven by an optimized voltage bias applied to the superconducting transition regime of the TES (Bender *et al.*, 2016).

### 2.2. SPT Circuit and fMux Readout

Each SPT-3G detector is connected to a circuit that consists of three main components: a SQUID, an inductor-capacitor filter network, and the wiring that connects all components. This circuit is shown in Figure 3. Each component is designed such that is minimizes parasitic resistance, which is important because excessive parasitic resistance will create a current biased TES which creates positive feedback and bolometer instability (Bender *et al.*, 2016).

SPT-3G utilizes a frequency domain multiplexing (fMux) readout system. In this scheme, each detector is biased at a unique location in frequency space and read out continuously to isolate resonant frequencies of the CMB (Bender *et al.*, 2016; Dobbs *et al.*, 2012). The fMux readout limits the thermal load on the 250

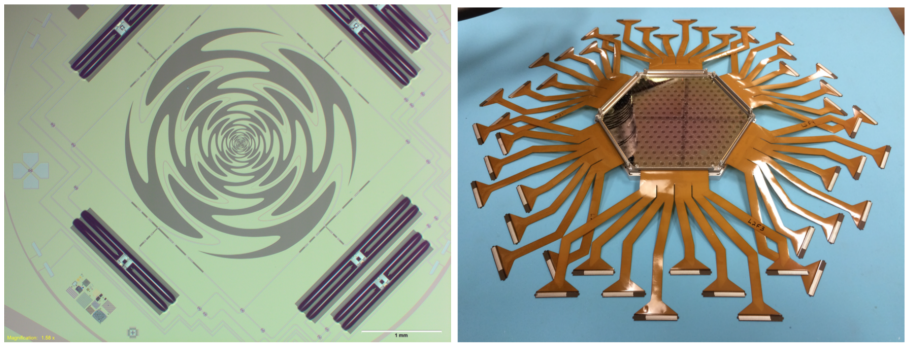

**Figure 2.** This figure shows: (left) the SPT-3G pixel with 6 TES, one pair for each frequency band of the CMB connected to a single antenna polarized for the 2 polarizations of the CMB. (right) An SPT-3G wafer with 271 pixels mounted for the fMux readout electronics.

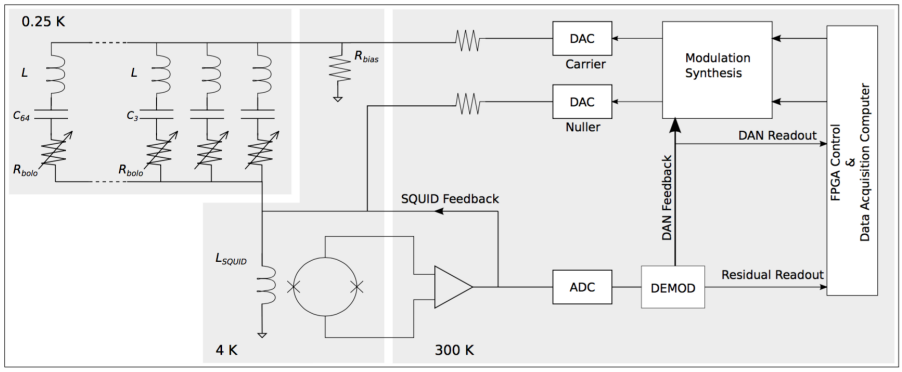


**Figure 3.** This figure shows a schematic diagram of the fMux circuit for SPT-3G. The gray boxes represent different operating temperatures of components.

mK cryogenic stage, reducing the required complexity of cold wiring (Dobbs *et al.*, 2012).

In the fMux scheme, each bolometer is assigned to a unique bias frequency and an array of 64 bolometers is simultaneously operated and read out on a single pair of wires. A parallel network of inductor-capacitor filters are wired in series with the bolometers and define resonant bands or a comb of resonant frequencies (Bender *et al.*, 2016). Single waveform AC biases are applied to the network and a single AC voltage bias is filtered for each bolometer. Millimeter wavelength signals from the CMB excite the detector antennae and modulate the TES resistance, which in-turn modulates the amplitude of the AC bias tone. The amplitude-modulated signal appears as sidebands in frequency around the AC bias tone. The current signals are then summed and input into a Superconducting Quantum Interference Device (SQUID) which provides low-noise amplification of the signal.

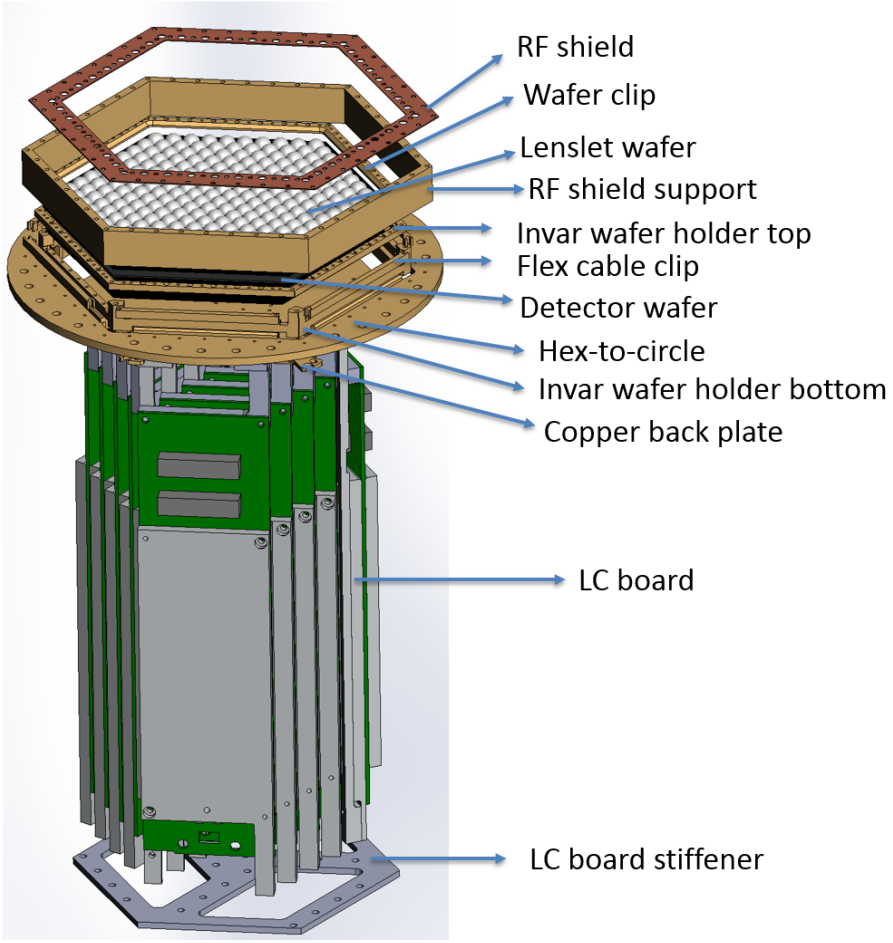


**Figure 4.** This figure shows a CAD diagram of the detector layout.

## 3. Testing of Superconducting Quantum Interference Devices

SQUIDs are sensitive devices used to detect fluctuating magnetic fields. The consist of a superconducting input coil and two Josephson junctions, which are weakly-linked superconductors placed on opposite branches of the superconducting input coil. The SQUID's voltage output is periodic when a magnetic field is applied across the ring and this flux is always an integer multiple of the flux quantum (Clarke and Braginski, 2006). SQUID technology has been widely used in circuits since the 1960s and they have a wide variety of applications. For the purposes of our circuit, SQUIDs were used primarily as transformers of input current and magnetic flux signal into output voltage signal and as amplifiers with a gain measured by their transimpedance (Clarke and Braginski, 2006). A series of eight SQUIDs operate with a room temperature op-amp to amplify the bolometer currents. The circuit is designed such that the input impedance is

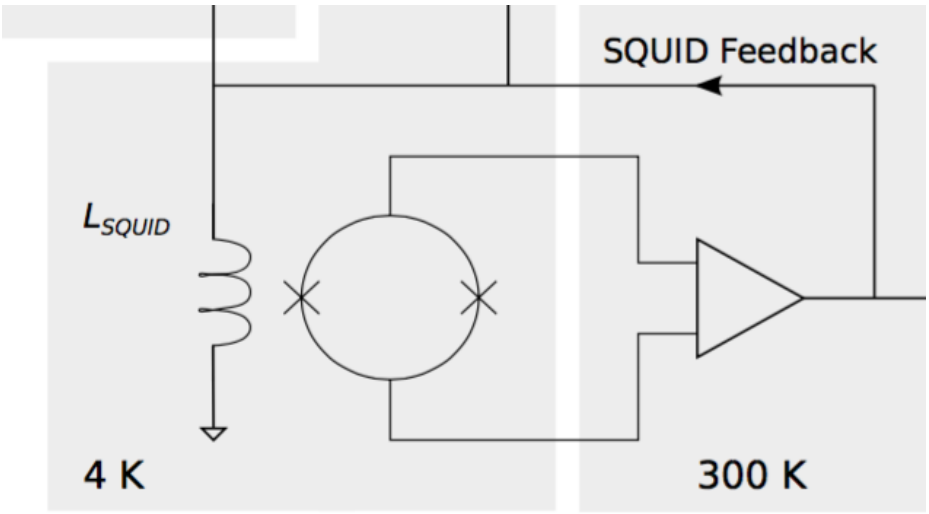


**Figure 5.** This figure shows the SQUID circuit we tested and used to generate Vphi curves. It should be noted that the SQUID circuit was isolated and no other detector circuit components were attached at this point.

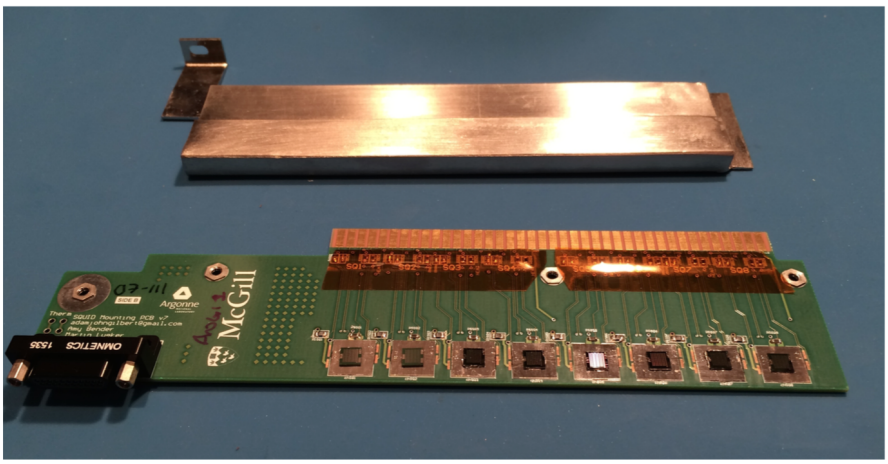


**Figure 6.** This figure shows a photograph of a superconducting quantum interference device (SQUID) board populated with eight SQUIDs next to its magnetic shielding.

low and does not affect bolometer voltage bias, transimpedance is large enough that output signals can be interfaced with the op-amp, and input noise is small compared to bolometer noise (Dobbs *et al.*, 2012).

### 3.1. Procedures

We tested seven custom mounting boards with eight SQUIDs each (65 SQUIDs in total). The boards were labeled as 08-200 through 08-206. Two types of SQUIDs were used in project: the SA13, which were on boards 200-201 and 204-206, and

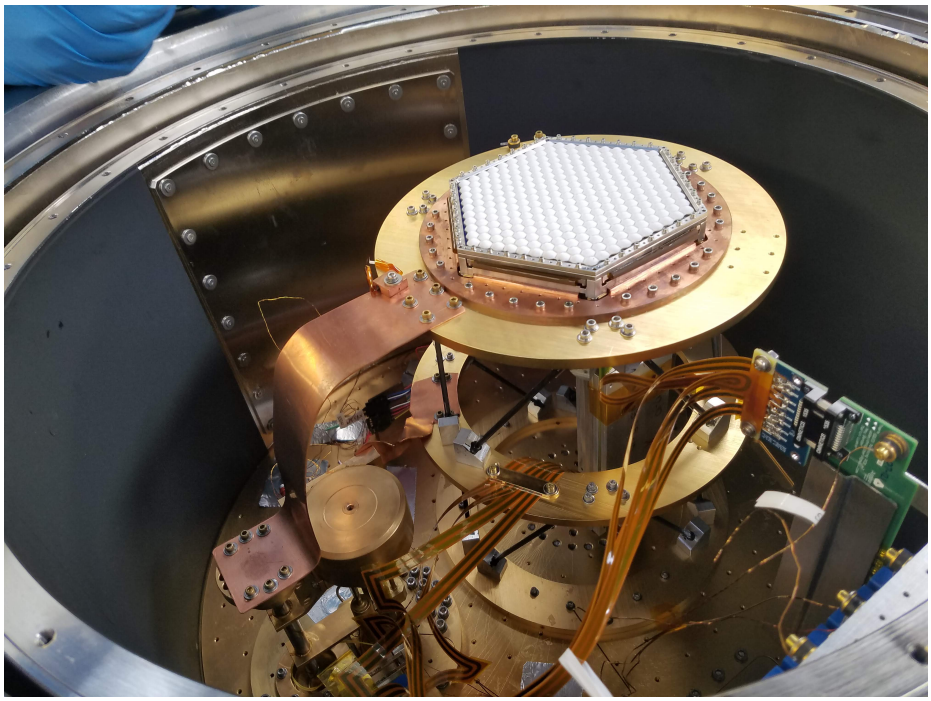

**Figure 7.** This Figure shows the cryostat setup in which we installed the SQUID Boards (bottom right) for testing.

the StarCryo, which were on boards 202 and 203 with one located on Mezzanine 2 Module 4 on board 201. The SA13 SQUIDs have been extensively used in previous SPT experiments and their behavior is well known. The StarCryo SQUIDs have not been used before and their performance was compared to the SA13s to supply feedback to their manufacturer. A diagram of the SQUID circuit is shown in Figure 5.

First, we used a microscope to read and record each SQUID serial number in a spreadsheet for reference. Next we secured the boards in magnetic shielding. This material absorbs electromagnetic field lines and would reduce their interference in SQUID operation. A SQUID board and its magnetic casing is shown in Figure 6. Next, we installed the SQUID boards in a cryostat, mounted them on the 2.5 K stage of the pulse tube cooler (PTC) as shown in Figure 7, and tuned the SQUIDs so that they operate at their optimum operating point. We used python algorithms entered in terminal to interface with the SQUIDs.

The first step in the tuning process was to heat the SQUIDs using a python algorithm. In this process, current was supplied to a heater resistor next to each SQUID, raising the devices temperature to its normal state and allowing it to cool quickly. This process reduced the probability of time varying field being transformed into spatially trapped flux and was repeated at the beginning of each test (Dobbs *et al.*, 2012).

Next, we mapped the SQUID output voltage response and generated "Vphi" curves using a python algorithm that works in the following way. The algorithm

input current biases, $I_b$, at the Digital-Analog Converter (DAC) though the SQUID's input coil. The preset parameters did not work for each SQUID so we changed them to range from 0.6 V to 1.1 V increasing in increments of 0.1 V. By convention, the program relays the current bias input in units of Volts. If so desired, the 4.22 $K\Omega$ nominal input resistor can be used to convert this information into units of Amps; however, this is not necessary for the purposes of this study. For each current bias $I_b$, the algorithm steps through values of flux bias, $I_f^i$ which is the current through the SQUID's input coil. Finally, the algorithm measures the voltage out of the op-amp at each $I_f^i$, and repeats the process.

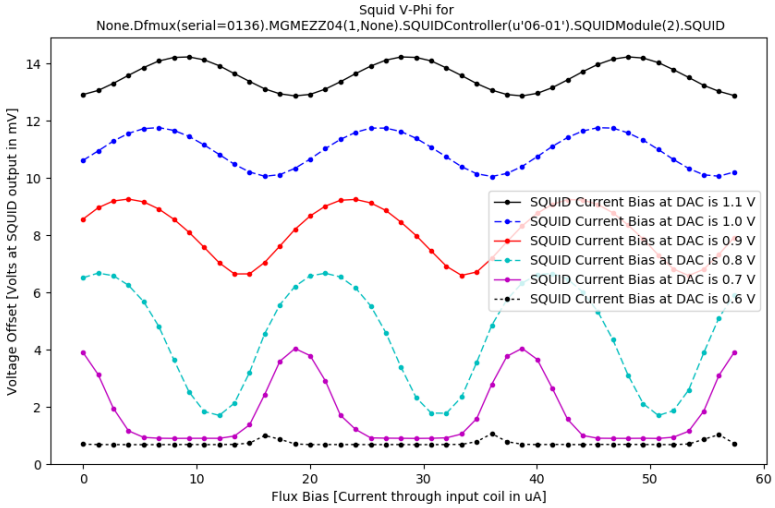


**Figure 8.** This figure shows an ideal Vphi curves for the SA13 SQUIDs

We visually checked each Vphi to ensure sure they behaved as expected. One of these curves for an SA13 is shown below in Figure 8. This Figure represents an ideal Vphi curve because the voltage offset vs flux bias are near perfect sinusoids whose amplitudes decrease as voltage offset increases. We use the Vphi curves to extrapolate data such as transimpedance and to choose which current bias optimizes SQUID performance.

Transimpedance, Z, defines the SQUID small signal response to changes in flux bias and it is the quantity that refers the room temperature electronics noise back to an equivalent noise current in the SQUID input coil (Dobbs *et al.*, 2012). Simply, transimpedance is a ratio of the output signal to the input signal, or a measurement of the amplifier's gain. Transimpedance is calculated by taking the derivative of the Vphi curve. Ideally, we want Z to be maximized for optimal SQUID performance. To calculate the optimal transimpedance, we ran a python algorithm that tuned the SQUIDs. Generally, any algorithm that tunes the SQUIDs finds the optimal current and flux bias that maximize Z. The optimal parameters are those that give a smooth Vphi curve with a high level of symmetry and steep slope.

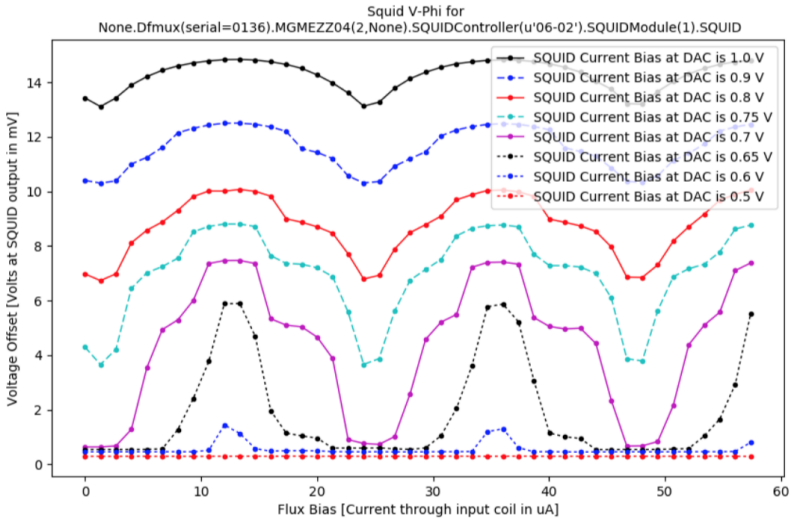


**Figure 9.** This figure shows a non-ideal Vphi curve.

A sinusoidal Vphi curve with the steepest slope represents the ideal current bias at which to operate the SQUID. For comparison, a non-ideal Vphi curve is shown in Figure 9. This curve is not ideal because its amplitude has a phi dependence and its curves are not smooth. In practice, this trait might not alter our data; however, each SQUID amplifies 64 channels and we have a large number of SQUIDs available. As a result, we can demand a higher quality of SQUID performance, even if the reasoning is pedantic.

We then used the Vphi data to extrapolate other behavioral characteristics of the SQUIDs.

### 3.2. Analysis and Discussion

We used the Vphi curves and data to calculate three sets of data: transimpedance, peak-to-peak voltage amplitude, and noise. Each data set characterized an important quality in SQUID operation.

After calculating the transimpedance of each SQUID, we generated the histogram shown in Figure 10 to analyze the overall performance of the system. In Figure 10, the StarCryo data points are shown in green and the SA13 data points are shown in purple. As shown in the graph, the StarCryo SQUIDs had a larger spread of transimpedance values and constituted all of the outliers in the data.

Based on the transimpedance data, several SQUIDs were removed from the final circuits and will not be used at the South Pole. The lowest accepted Z threshold SQUIDs on SPT can have is 400 Ω because SQUIDs tested with a transimpedance below this threshold had too low of a gain and too much noise resulted in the reading. As seen in Figure 10, four SQUIDs fall below this range

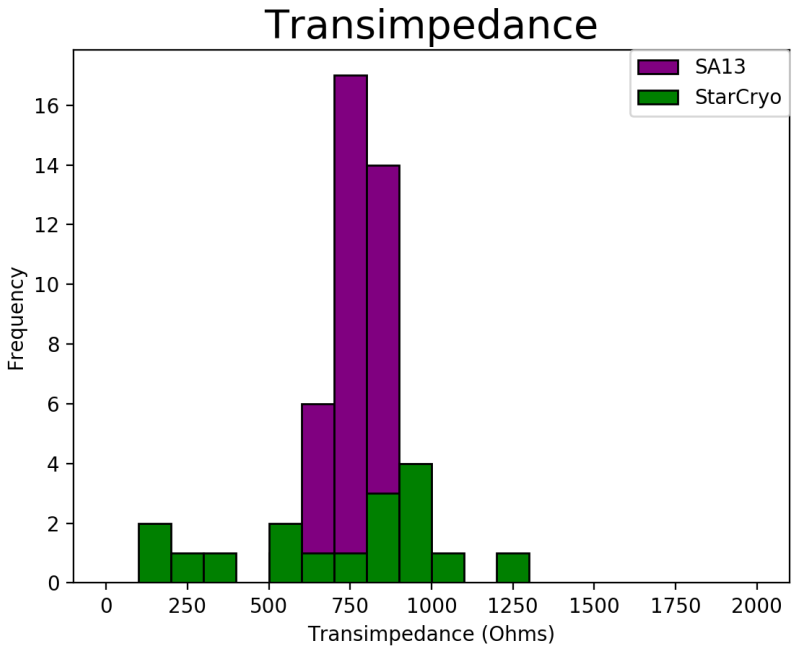


**Figure 10.** This figure shows a histogram of the transimpedance values for all of the SQUIDs.

and were recorded for removal or further inspection. One SQUID on board 205 did not give a transimpedance value most likely due to a broken wirebond or defective SQUID. This SQUID was also recorded for further inspection.

Next, we calculated the peak-to-peak voltage amplitude, Vpp, of each SQUID and characterized the data using the histogram shown in Figure 11. This data represents the SQUID's large signal response where distance between the max and min peaks in each Vphi curve is the current required to produce a flux quantum through the SQUID coil independent of bias current (Dobbs *et al.*, 2012). We took this measurement as a consistency check for the transimpedance values as a SQUID with a high transimpedance (slope) should also yield a large Vpp (distance from peak to trough).

Finally, we measured the SQUID output voltage noise. We collected the noise data by measuring the output voltage at the op-amp for a few milliseconds at a data rate of 20 MHz. Next, the algorithm measured the Power Spectral Density (PSD). We took the median noise value for each SQUID and graphed them in the histogram shown in Figure 12. This graph showed the noise of the output voltage of the op-amp. As shown in Figure 12, the StarCryos had a larger spread in their noise data and the noise of all SQUIDs centered just above 0.002 $\mu$V/rtHz

In addition to the output voltage noise, we computed the input current noise of the SQUIDs. Current, voltage, and transimpedance are related by the following equation:

$$IZ = V$$

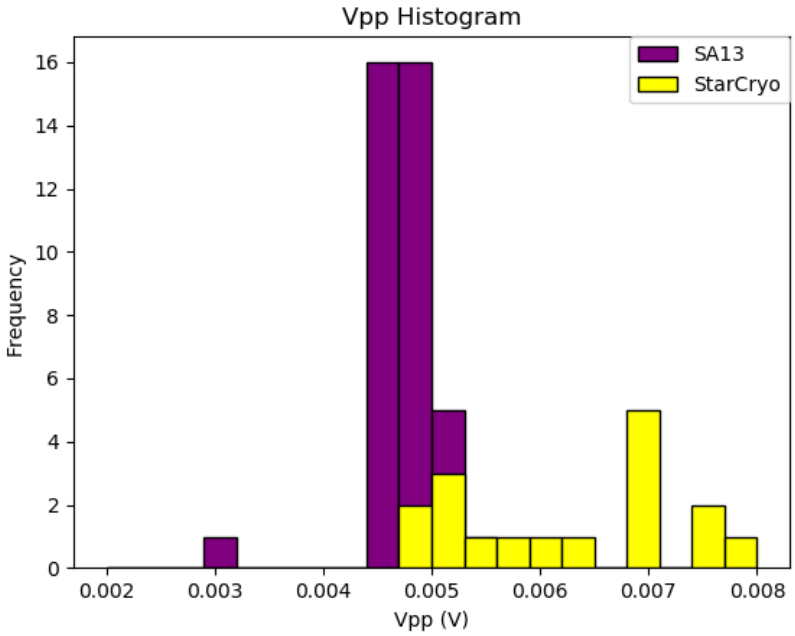


**Figure 11.** This figure shows the histogram of the vpp data

We converted the voltage noise data into current noise data by dividing the voltage noise by the SQUID's transimpedance. This data was then graphed in Figure 13. This noise data is tighter than the output voltage noise. This is because the differing values of Z for each SQUID scale the noise by a different factor. By dividing out Z, the noise is scaled by the same factor. As shown in Figure 13, the noise values are around 5 pA$/\sqrt{Hz}$. For the detector circuit, the current noise is expected to be around 15-20 pA$/\sqrt{Hz}$; however, because the SQUID circuit was isolated for this portion of testing, the range of noise shown in Figure 13 is acceptable.

Out of 56 SQUIDs, 5 were excluded because they were defective or did not meet the specifications set for use on SPT-3G. This data yields an 8.9 percent failure rate with the SQUIDs. Moreover, we found that the StarCryos had a larger distribution in noise and transimpedance data. We will send this feedback to their manufacturer to help them as they continue to develop their SQUID technology.

## 4. Testing of Inductor-Capacitor Filter Network

The resonant filter networks, as shown in the circuit diagram in Figure 14. The LC network of 68 device pairs and wiring is monolithically fabricated on a chip, each of which has three components. These components include an aluminum

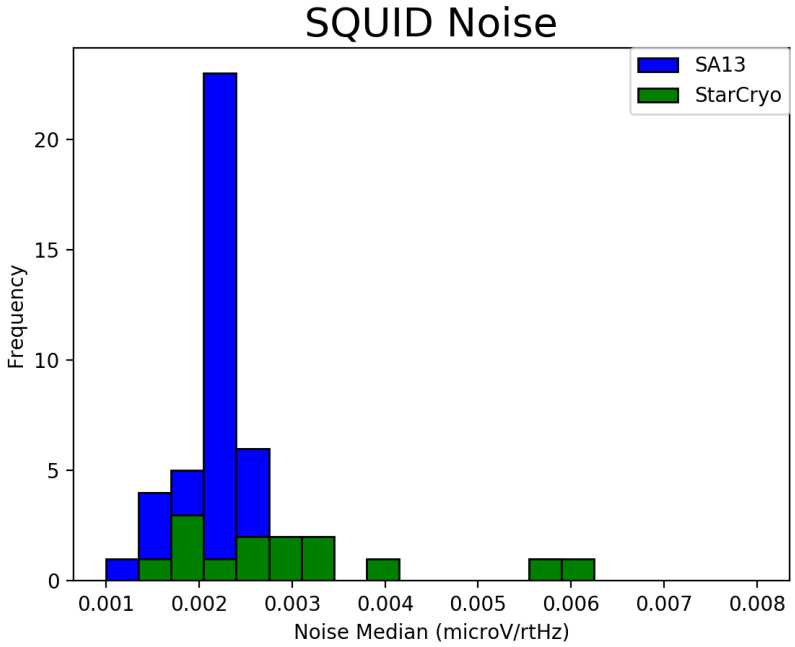


**Figure 12.** This figure shows a histogram for the mean output voltage noise values of the SQUIDs. Notice the StarCryo SQUIDs again have a larger spread in noise data.

backing layer, silicon dielectric, and an aluminum layer with patterns of inductors and capacitors as show in Figure 15 (Bender *et al.*, 2016).

The SPT-3G focal plane consists of a total of 240 filter networks, or 120 LC boards that operate at a temperature of 250 milliKelvin. Each filter network connects to 66 bolometers the best-performing of which can be chosen to run the detector (Bender *et al.*, 2016).

### 4.1. Procedures

The filter network functions in the fMux multiplexing by separating the incoming signal by frequency and sending it down each branch of the "comb." For this stage of the project, we tested to ensure that the LC boards worked and to identify the optimal frequencies at which to operate them. To accomplish this goal, we took a net analysis of the circuit using a python algorithm. A net analysis is used to analyze a complicated circuit. Typically, a signal is input into the circuit at a certain frequency. The signal is measured at the circuit's output and the network analysis is given by the ratio of signal output to signal input. The signals are made such that the input and output have the same amplitude, making the analysis independent of amplitude. The program then sweeps through a range of frequencies and identifies peaks. Each bolometer is operated at the frequency that maximizes the carrier-to-nuller ratio.

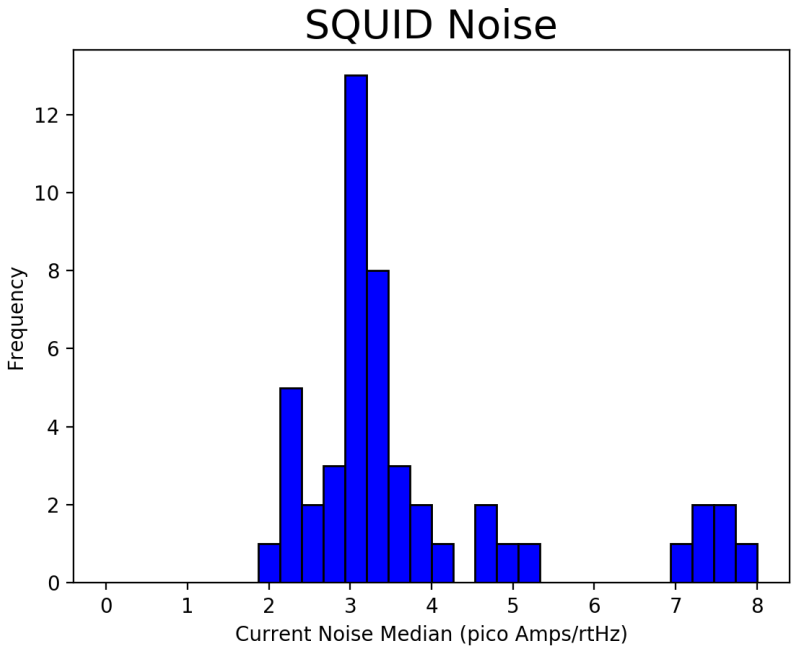


**Figure 13.** This figure shows a histogram for the mean current noise values of the SQUIDs.

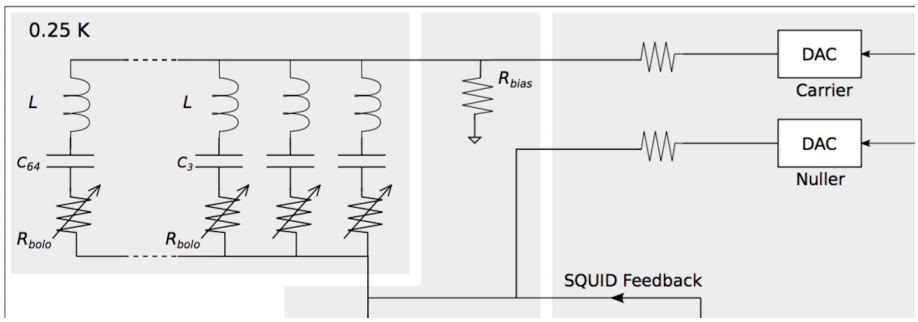


**Figure 14.** This figure shows a circuit diagram of the LC resonant filtering network.

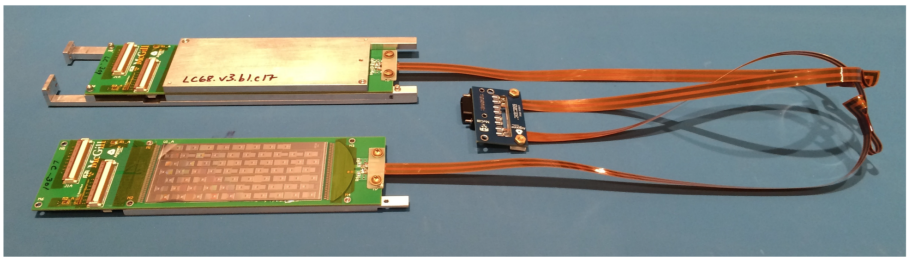

**Figure 15.** This figure shows a photograph of two inductor-capacitor board with cryogenic wiring.

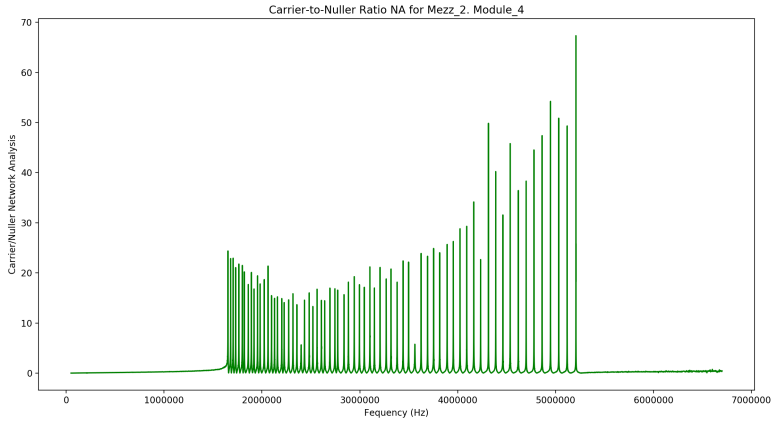


**Figure 16.** This figure shows the Network Analysis graph of the Carrier-to-Nuller ratio frequencies.

This particular filter network relies on two input signals, the carrier and the nuller. As a result, we run two network analyses, one for each input signal. After running a network analysis for each signal, we took the ration of the carrier to nuller signals and generated the graph shown in Figure 16. The circuit usually operates with SQUID feedback as show in Figure 14 which creates a virtual ground at that point. Taking the ratio of these input signals simulates these conditions under which the circuit will operate at the South Pole. Next, the algorithm identified peaks in the graphs and marked them with a dashed line as shown in Figure 17.

Upon initial visual inspection, we noticed that, in some graphs, the algorithm did not identify all of the peaks present and, as a result, did not record these peaks. This was most likely due to a slight non-uniformity in performance across the LC boards. To ensure the algorithm identified all peaks, we altered its parameters. We increased the width of the curve the algorithm identifies as peaks and decreased the signal-to-noise ratio which results in smaller curves being considered peaks.

Finally, we calculated the spacing between individual frequency peaks. We want the LC resonant frequencies to be sufficiently far apart to prevent the likelihood of crosstalk in the data. Crosstalk in the signal would occur if two or more resonant frequencies were too close that their LC filters registered multiple signals as having that frequency. The frequency spacing depicted in Figure 18 is ideal because it shows that the peaks are separated by at least 20 kHz and that the spacing increases as the frequency increases.

## 5. Conclusions

We found that SQUID transimpedance and noise values were acceptable for deployment at the South Pole. Ultimately, five SQUIDs did not meet tran-

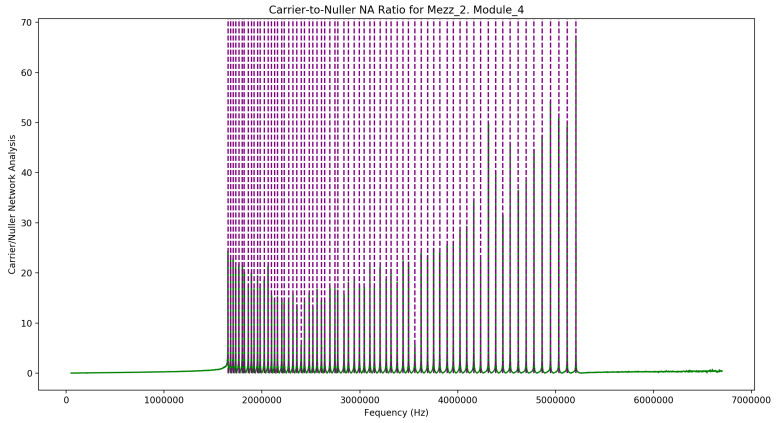


**Figure 17.** This figure shows the Carrier to Nuller Network Analysis graph from Figure 16 with dotted lines identifying the frequencies of optimized performance.

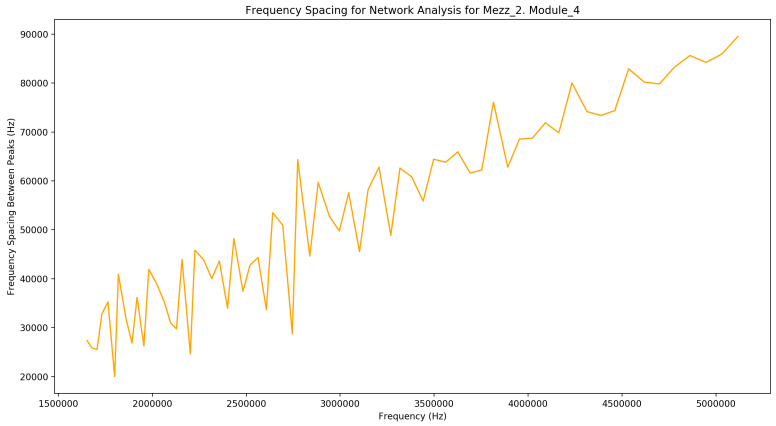


**Figure 18.** This figure shows a graph of the frequency spacing of the peaks from Figure 16.

simpedance constraints and were removed from further use. All LC boards passed our analyses and the ideal frequencies at which to operate them for optimal detector performance were identified. These components will be transported to the South Pole during the next Austral Summer for deployment on the SPT.

Additionally, we analyzed the StarCryo SQUID performance compared to the more developed SA13s. Compared to the SA13s, StarCryos exhibited a wider range in transimpedance and noise values, making them less precise. This data will be sent to the StarCryo company as feedback so they can continue to improve their product and potentially become another source of SQUIDs for the collaboration.

## 6. Acknowledgments

Before concluding, I would like to take the time to say thank you to people who have helped me throughout this summer. First, thank you to my supervisors Bradford Benson, Sasha Rahlin, Adam Anderson, and Donna Kubik for taking the time to teach me the concepts and skills to complete this project and prepare me for others. Thank you to my mentors: Charlue Orosco, Alex Drlica-Wagner, and Matt Alvarez for helping me prepare my paper and presentation. Thanks to Josemanuel Hernandez for being an incredible friend and person to work with. Finally, I would like to give an enormous thank you to Fermilab and the SIST committee for giving me this opportunity and funding my project. This has been an incredible summer of learning and growth and I and grateful for it.

## References

Bender, A., Ade, P., Anderson, A., Avva, J., Ahmed, Z., Arnold, K., Austermann, J., Thakur, R.B., Benson, B., Bleem, L., *et al.*: 2016, Integrated performance of a frequency domain multiplexing readout in the spt-3g receiver. In: *Millimeter, Submillimeter, and Far-Infrared Detectors and Instrumentation for Astronomy VIII* **9914**, 99141D. International Society for Optics and Photonics. [bender2016]

Benson, B., Ade, P., Ahmed, Z., Allen, S., Arnold, K., Austermann, J., Bender, A., Bleem, L., Carlstrom, J., Chang, C., *et al.*: 2014, Spt-3g: a next-generation cosmic microwave background polarization experiment on the south pole telescope. In: *Millimeter, Submillimeter, and Far-Infrared Detectors and Instrumentation for Astronomy VII* **9153**, 91531P. International Society for Optics and Photonics. [benson2014]

Carlstrom, J.E., Crawford, T.M., Knox, L.: 2018, Particle physics and the cosmic microwave background. *arXiv preprint arXiv:1805.06452*. [carlstrom2018]

Clarke, J., Braginski, A.I.: 2006, *The squid handbook: Applications of squids and squid systems*, John Wiley & Sons, ???. [clarke2006]

Dobbs, M., Lueker, M., Aird, K., Bender, A., Benson, B., Bleem, L., Carlstrom, J., Chang, C., Cho, H.-M., Clarke, J., *et al.*: 2012, Frequency multiplexed superconducting quantum interference device readout of large bolometer arrays for cosmic microwave background measurements. *Review of Scientific Instruments* **83**(7), 073113. [dobbs2012]

Krauss, L.M., Dodelson, S., Meyer, S.: 2010, Primordial gravitational waves and cosmology. *Science* **328**(5981), 989. [krauss2010]